

Flexible Seaweed-Like Triboelectric Nanogenerator as a Wave Energy Harvester Powering Marine Internet of Things

Yan Wang,[‡] Xiangyu Liu,[‡] Yawei Wang,[‡] Hao Wang, He Wang, Steven L. Zhang, Tiancong Zhao, Minyi Xu,^{*} and Zhong Lin Wang^{*}



Cite This: *ACS Nano* 2021, 15, 15700–15709



Read Online

ACCESS |



Metrics & More



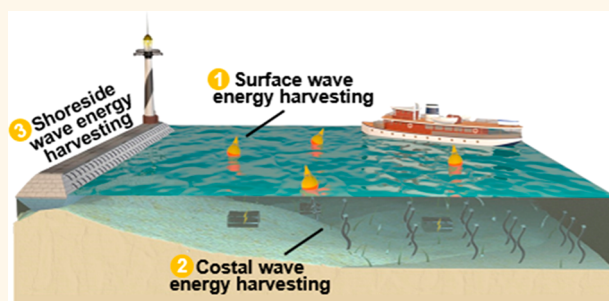
Article Recommendations



Supporting Information

ABSTRACT: The marine internet of things (MIoT), an increasingly important foundation for ocean development and protection, consists of a variety of marine distributed sensors under water. These sensors of the MIoT have always been highly dependent on batteries. To realize *in situ* power supply, a flexible seaweed-like triboelectric nanogenerator (S-TENG) capable of harvesting wave energy is proposed in this study. The flexible structure, designed with inspiration from the seaweed structure, processes extensive marine application scenarios. The bending and recovering of the S-TENG structure under wave excitations are converted to electricity. As the output performance increases with the number of parallel connected S-TENG units, an S-TENG system with multiple units could serve for floating buoys, coastal power stations, and even submerged devices. Through the demonstration experiments performed in this study, the flexible, low-cost S-TENG could become an effective approach to achieve a battery independent MIoT.

KEYWORDS: triboelectric nanogenerator, wave energy harvesting, marine internet of things, bionic, self-powered



The marine internet of things (MIoT) has become increasingly important in ocean development and protection through a sensor network distributed at the ocean surface, under water, or on the coast.^{1–4} Various sensors measure a variety of parameters, which include wave record, tide record, sonic record, current profile, turbidity, salinity, pH, pressure, temperature, radiation, conductivity, *etc.* So far, these sensors have been highly dependent on batteries, which means they need to be collected, recharged, and replaced from time to time. As the MIoT is expanding to full functionality, the corresponding cost and labor would increase so rapidly that people are thinking of alternatives to charge the batteries by harvesting *in situ* energy to power the marine distributed sensors.

The realization of *in situ* power supply for the distributed sensors is a serious challenge.⁵ Renewable energies, like solar energy and wind energy, have been utilized to power these sensors on land. However, they are not capable of covering the large number of underwater applications, which make up much of the MIoT. As the “native” energy in the ocean, wave energy is more desirable for powering the MIoT due to its extensive availability and high density (order of magnitude higher compared to solar or wind).⁶ Currently, the most demonstrated commercial ocean wave energy converters are based on

the traditional electromagnetic generators (EMGs).^{7,8} Although the EMG wave energy converters operate efficiently in their design sea states,^{9–12} they share the common disadvantage of low efficiency under low frequency conditions.^{13–15} The ever-changing, random marine environments are a serious challenge to their robustness.

The triboelectric nanogenerator (TENG) has been revolutionary in efficiently converting micro mechanical energy to electricity, and (relative to other energy converters) it accompanies less environmental risks.^{16–29} Compared with the electromagnetic generators, the TENG has significant advantages in harvesting low-frequency energy.^{30–34} Recently, a few triboelectric nanogenerators (TENGs) have been proposed for harvesting ocean wave energy.^{13,34–45} Xu *et al.*⁴⁶ has developed a tower-like TENG (T-TENG) for harvesting water wave energy from six degrees of freedom,

Received: June 16, 2021

Published: September 16, 2021



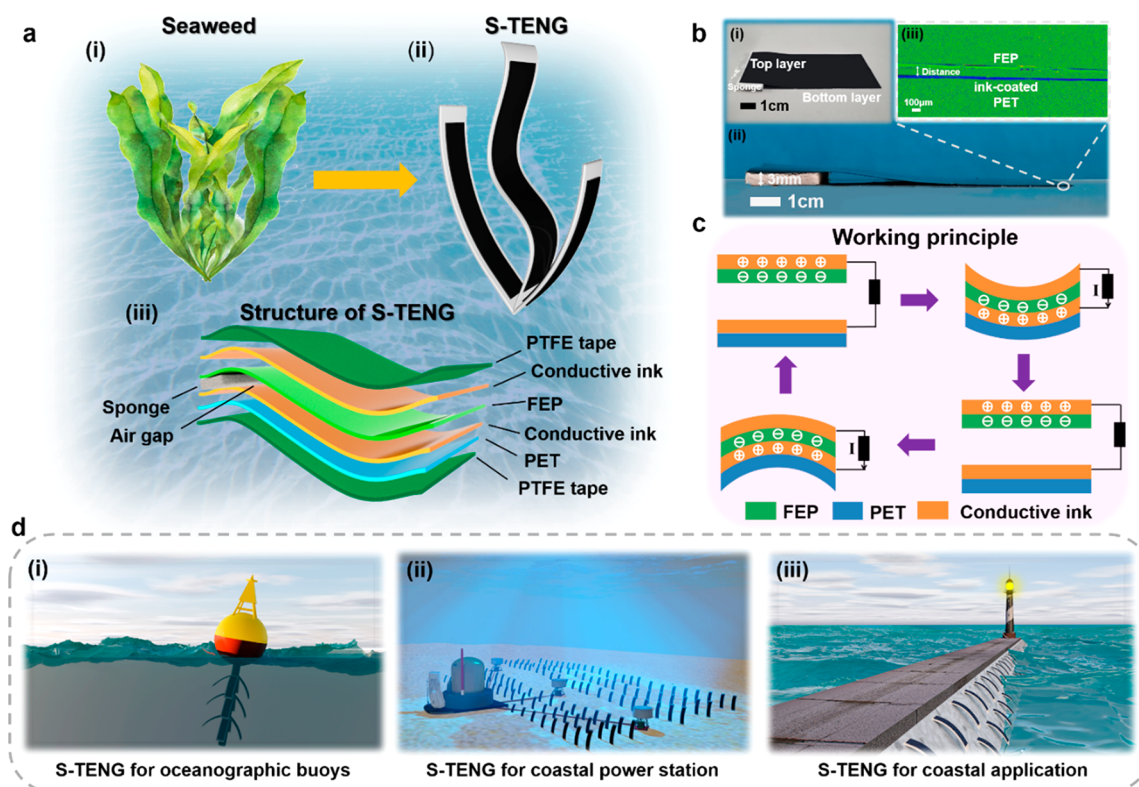


Figure 1. Schematic drawing of the S-TENG and its applications: (a, i) seaweed, the bionic prototype of the S-TENG; (a, ii) the S-TENG profile; (a, iii) the S-TENG internal structure. Photos of the S-TENG (b, i) and (b, ii) side view of it, and (b, iii) side view of the material surface morphology on the S-TENG. (c) Working mechanism of the S-TENG. (d) Applications of the S-TENG on the marine internet of things.

random wave induced motions. The T-TENG appears to be a quite effective approach of large-scale wave energy harvesting. An *et al.*⁴⁷ have created a whirling-folded TENG (WF-TENG) wave energy converter. Variations of output performances with respect to the wave parameters and the structural parameters were investigated systematically. A maximum peak power of 6.5 mW and an average power of 0.28 mW were obtained by the WF-TENG, which is capable of powering a digital thermometer. In a study on a fully enclosed TENG wave energy converter published by Wang *et al.*,¹³ optimizations of materials and structures were conducted. Low frequency wave energy was converted to power light-emitting diodes (LEDs) and to charge different supercapacitors to the rated voltage.

In general, these published wave energy TENGs have exhibited advantages such as having a simple structure and low cost and being lightweight and robust. However, most of the previously published wave energy TENGs are designed for harvesting energy from the ocean surface waves. Though the majority of the marine applications are surface ones, supplying renewable electricity to underwater applications should not be left out. In order to encompass energy harvesters in a larger volume of the ocean to provide power to the MIoT sensors, a wave energy TENG that can work at both surface areas (floating) and underwater areas (submerged) is desperately needed. On top of that, the wave energy TENG will be more impressive if it can be easily integrated with the marine equipment.

In this study, a flexible seaweed-like triboelectric nanogenerator (S-TENG) is first proposed to supply *in situ* power to marine distributed sensors. The idea of developing a seaweed-like TENG is inspired because of the close

observations we made on a common sea plant, seaweed. The process in which the seaweed vibrates with the wave is a process of converting wave energy to mechanical energy. The flexible S-TENG converts the wave energy into electricity through its distinctive structure. Systematic wave tank experiments were performed to study the vibration and electric characteristics of the S-TENG under various geometric and dynamic parameters. Multiple S-TENGs have been tested to power either the LEDs or the thermometer in different marine scenarios. Considering that the majority of the MIoT sensors work with micro power, the S-TENG could become an effective approach of powering a variety of marine sensors in the MIoT.

RESULTS AND DISCUSSION

Structure and Working Principle of the S-TENG. The bionic prototype that inspired us to develop the seaweed-like structure to harvest wave energy is shown in Figure 1a(i). From the observation that the seaweed vibration has converted much of the wave kinetic energy successfully to heat, a flexible seaweed-like triboelectric nanogenerator is first proposed (see Figure 1a(ii)). As shown in Figure 1a(iii), the S-TENG is made by a conductive ink-coated fluorinated ethylene propylene (FEP), a conductive ink-coated polyethylene terephthalate (PET), and two polytetrafluoroethylene (PTFE) membranes. Sealed inside the PTFE layer, the triboelectric friction layers, the FEP and PET membranes, are protected from any contact with water that would cause the electric materials to lose their surface charge. Figure 1b(i) displays the S-TENG sample. To further show the air gap between two triboelectric layers, the photo of the side view of

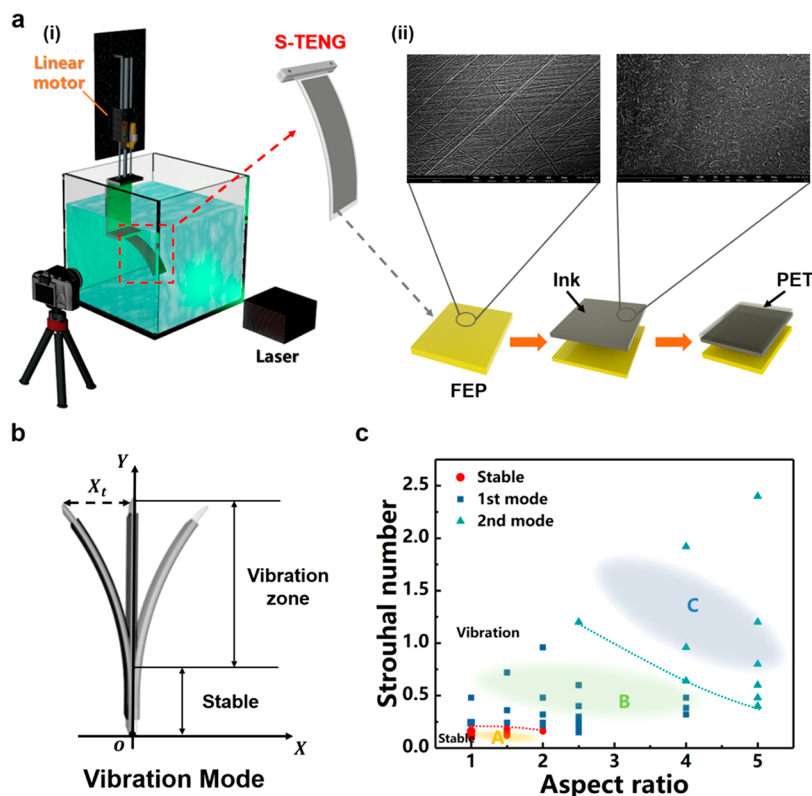


Figure 2. Experimental apparatus and vibration characteristics of the S-TENG. (a, i) Experimental apparatus of the S-TENG; (a, ii) scanning electron microscope (SEM) photo of the FEP and conductive ink-coated PET; (b) 1st mode of the S-TENG and coordinate system selection diagram; (c) the vibration regime map of the S-TENG.

the sample is taken in Figure 1b(ii) and the micro view is measured by the electron microscope LEXT OLS4000, which is shown in Figure 1b(iii). From above, the air gap due to the sponge and surface morphology of the FEP and ink-coated PET film can be observed. The device (Figure S1) with concave structures makes contact electrification and electrostatic induction simultaneously, ensuring a good correspondence between the wave and electrical signal of the S-TENG. It is better to set the two triboelectric layers to “contact” state initially so that the TENG could produce output even with minor excitation.⁴⁸ When an incident wave is present, two triboelectric layers are brought into contact with each other, and the contact area correlates with the wave excitation.

As the S-TENG vibrates periodically under the wave excitations, the FEP membrane will make contact with and separate from the PET membrane periodically as shown in Figure 1c. After certain contacts with the ink-coated PET, the FEP membrane will become negatively charged. According to the essence of electrostatic induction, an equivalent amount of positive charge will occupy the ink electrode on the PET when the ink electrodes of PET and the FEP membrane have sufficient contact. As the S-TENG bends, the electrons will flow from the electrode attached to the FEP to the electrode attached to the PET (through the external circuit); therefore, a transient current is generated. Subsequently, as the FEP and ink electrode get separated, the positive charges will flow back to the upper electrode. Due to its high Young’s modulus as well as its good ink adhesion characteristics, the PET material is selected for the other triboelectric friction layers for the S-TENG. A coordinate system is defined to better clarify the geometry of the S-TENG, as displayed in Figure S2. The

governing equation for the S-TENG can be derived on the basis of a contact-mode TENG,⁴⁹ which can be written as

$$V = -\frac{Q}{\epsilon_0 S}(d_0 + y(t)) + \frac{\sigma y(t)}{\epsilon_0} \quad (1)$$

where Q is the total transferred charge; d_0 , ϵ_0 , and S represent the thickness of the membrane, the dielectric constant in vacuum, and the area size of the electrode, respectively; y denotes the displacement between the dielectric membrane and the electrode; σ denotes the charge density. According to the eq 1, the maximum displacement between the dielectric membrane and the electrode determines the maximum output of the S-TENG. The displacement between the dielectric membrane and the electrode changes as the S-TENG vibrates with the wave.

To better show the working principle of the S-TENG, the potential distributions across the two electrodes have been analyzed with COMSOL, a finite-element software for Multiphysics analysis as shown in Figure S3. The contour clearly depicts the potential difference driving the current between the two electrodes. Owing to its flexible essence, the S-TENG can be applied (as a power supply module) to many marine applications, such as floating buoys (surface), coastal power stations (underwater), and breakwaters (shoreside), as shown in Figure 1d.

Vibration and Electric Performance of the S-TENG. As shown in Figure 2a(i), a linear motor was used to simulate the vibration of the S-TENG excited by the wave, and laser imaging was adopted to better observe the vibration performance of the S-TENG. The microstructure of the FEP and ink-coated PET film can be observed by a scanning electron

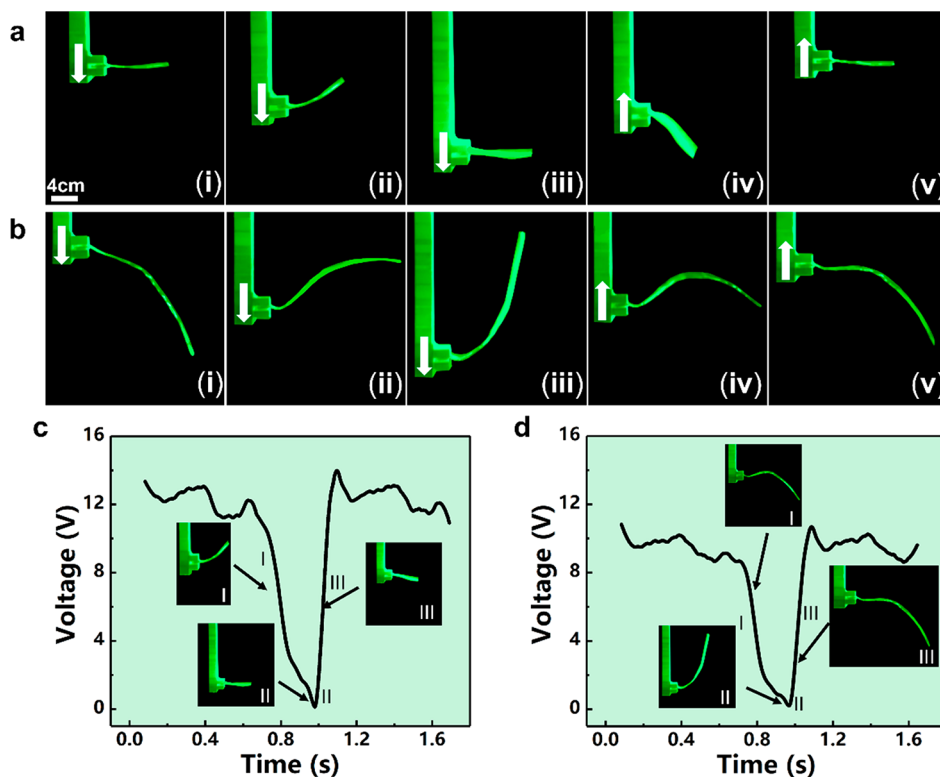


Figure 3. Sequential images of vibration behavior and analysis of the electrical signal for the 1st mode. (a) 1st mode: vibration behavior of the S-TENG with the dimensions 40×80 mm; (b) 2nd mode: vibration behavior of the S-TENG with the dimensions 40×200 mm. The voltage signal of the S-TENG corresponding to (c) the 1st mode; (d) the 2nd mode.

microscope Phenom Pro image as shown in Figure 2a(ii). The device with concave structures made contact electrification and electrostatic induction simultaneously, ensuring a good correspondence between the wave and electrical signal of the S-TENG. Certain nondimensional parameters have been applied to represent elasticity and fluid pressure on the structure. The length (l) is usually expressed by the nondimensional aspect ratio l/w ,⁵⁰ where w is the width of the S-TENG. The vibration frequency (f) is usually expressed by the Strouhal number ($S_t = fl/U$).

The S-TENG's vibration under the wave excitation is a typical forced vibration. The S-TENG can be approximated as a thin two-dimensional structure with high extensional rigidity and low bending rigidity, which satisfies the Euler–Bernoulli beam equation⁵¹

$$m\partial_t^2\omega + D\partial_Y^4\omega = -\Delta p \quad (2)$$

where m is the mass per unit area, D is the nondimensional bending stiffness of the structure, ω is the displacement of the S-TENG along the X -coordinate, and Δp is the hydrodynamic pressure difference, which is induced by the waves across the structure. Among these parameters, the nondimensional bending stiffness (D) is what governs the vibration of a thin two-dimensional structure (e.g., the S-TENG).^{52,53} D is defined as

$$D = \frac{Eh^3}{12(1-\nu^2)\rho_f U^2 L^3} \quad (3)$$

where ν is the Poisson's ratio, ρ_f is the fluid density, U is the wave velocity, h is the thickness of the S-TENG, L is the structure length, and E is the Young's modulus. Since the

bending stiffness (D) largely determines the deformation of the S-TENG, D will eventually affect the electric performance of the S-TENG. Considering that the fluorinated ethylene propylene (FEP) has a relatively low Young's modulus and high electronegativity, it was selected as the dielectric material in the S-TENG.^{54,55} The corresponding material parameters are listed in Table S1. Equations 2 and 3 are the governing equations that determine the coupled fluid and structural motion of the S-TENG depicted in Figure 2b.

One key parameter to evaluate the second order oscillation is the Strouhal number. In the experiments, the Strouhal number was increased from 0.08 to 2.4. The physical dimensions for the experimental samples are listed in Table S2. Figure 2c is the two-dimensional map characterizing the vibration status with respect to the dimensionless parameters. The S-TENG stayed stable when the Strouhal number was within 0.18, and the aspect ratio ranged from 1 to 2. As the Strouhal number and the aspect ratio increased, the S-TENG exhibited the first mode characteristic of a cantilever beam,⁵⁶ as shown in Figure 2b. The vibration amplitude of the lower part was nearly zero, while the upper part was the vibration zone with the vibration amplitude increasing toward the trailing edge. As the Strouhal number and the aspect ratio increased further, the vibration gradually transitioned from the first mode (region A) to the second mode (region B). The transition between the first mode and second mode appeared when the Strouhal number ranged from 0.4 to 1.2 and the aspect ratio ranged from 2.5 to 5, as shown in Figure 2c. The S-TENG's vibration is excited by the wave. Theoretically, the vibration frequency equals the wave frequency. According to the experimental results in Figure 2c, when the aspect ratio is constant, the vibration mode is determined by the Strouhal

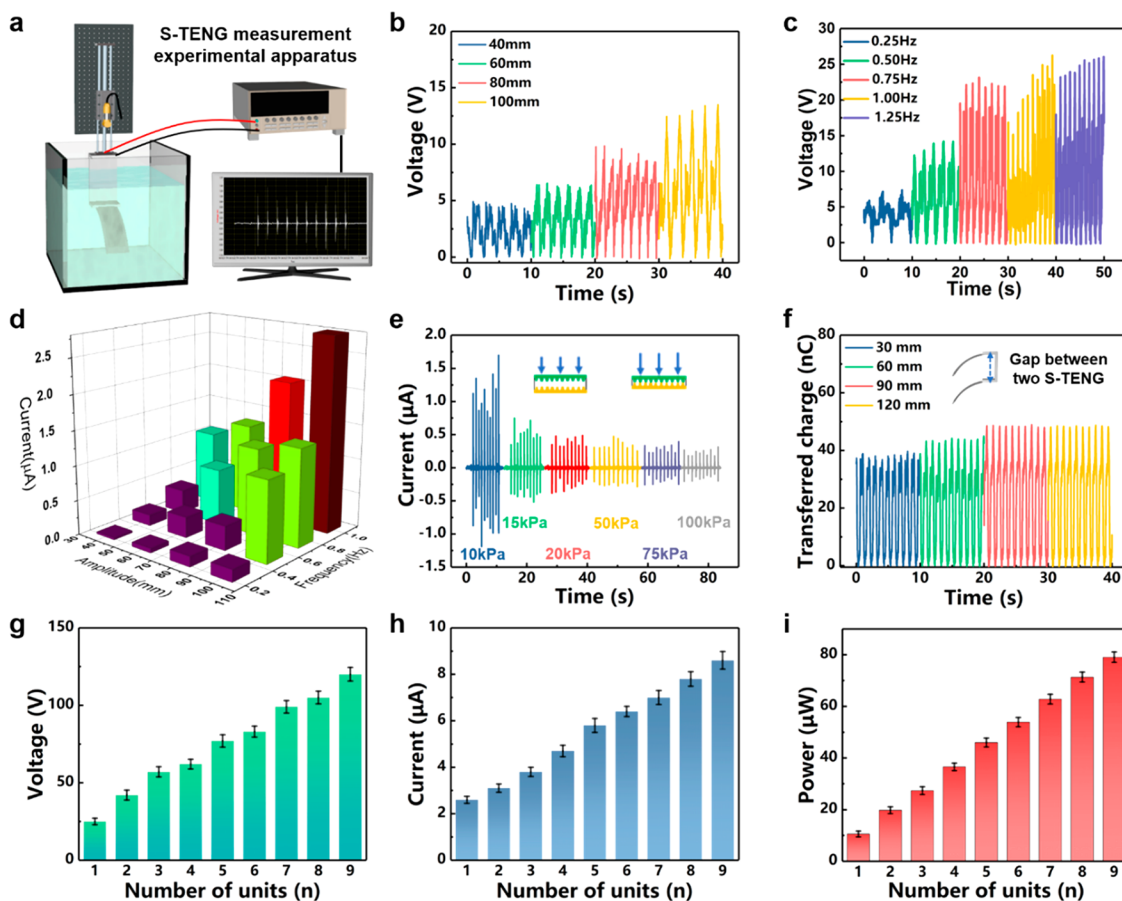


Figure 4. Output performances of the S-TEG. (a) Experimental apparatus of the S-TEG; (b) the effects of the linear motor's motion amplitude on the open-circuit voltage of the S-TEG; (c) the effects of the frequency of the linear motor on the open-circuit voltage of the S-TEG; (d) a 3D graph of the output current under different amplitudes and frequencies of the linear motor; (e) the output current of the S-TEGs under different pressures; (f) the transferred charge of the S-TEG with different parallel distances; (g) the output voltage of the S-TEGs with different numbers of units; (h) the output current of the S-TEGs with different numbers of units; (i) the output power of the S-TEGs with different numbers of units.

number. The dimension will influence the vibration mode but not the vibration frequency.

Figure 3a,b presents the sequential images of the first mode vibration and second mode vibration. In the first mode for the S-TEG, only one vibration crest occurred during the whole vibration process. The S-TEG is horizontal on its equilibrium condition (Figure 3a(i)). In the first half of a vibration cycle, the S-TEG first reaches the largest upward displacement (Figure 3a(ii)); then, the S-TEG returns back to the horizontal equilibrium position (Figure 3a(iii)). In the remaining half cycle, the S-TEG reaches the largest downward displacement (Figure 3a(iv)) before it returns back to the horizontal equilibrium position (Figure 3a(v)). The periodic vibration leads to periodic contact separation between the internal dielectric material and the electrode. The process of the second mode vibration (see Figure 3b) is similar to the process of the first mode vibration except that there are two vibration crests in the second mode. When the profiles of the electrical signal and the vibration images are scrutinized, it can be observed that the vibration of the S-TEG yielded the following stages: starting to vibrate (Figure 3c(I)), reaching the maximum stroke (Figure 3c(II)), and returning to the original condition (Figure 3c(III)). These stages were also clearly reflected in the corresponding output voltage signals. The similar voltage signal can be observed in Figure 3d. However,

the maximum output voltage of the second mode is lower than the first mode. It is likely that the triboelectric electrons generated by the two opposite crests cancel out each other, which reduces the electric output of the S-TEG. Therefore, the first mode S-TEG turns out to be better for energy conversion.

As our studies have shown that the 40 × 80 mm S-TEG can be excited to the first mode under a wide range of Strouhal numbers (see Figure 2c), experiments on the S-TEG's electric performance were carried out with the 40 × 80 mm S-TEG dimension. The forced motion is generated by the linear motor reciprocating sinusoidally. The experimental apparatus is shown in Figure 4a. As shown in Figure 4b, larger motion amplitude can promote the output electrical signal: a maximum output voltage of 12.2 V was achieved with the transferred charge of 22.4 nC (Figure S4). The output performance of the S-TEG is also positively correlated with the vibration frequency (Figure 4c): at the maximum wave frequency of 1.25 Hz, the open-circuit voltage reached 24.8 V with the transferred charge of 43.2 nC (Figure S5). A series of experimental results were compiled, and Figure 4d presents the dependence of the output current on both the amplitude and the frequency of the S-TEG. The output current can be greatly enhanced by increasing the amplitude and frequency of the S-TEG.

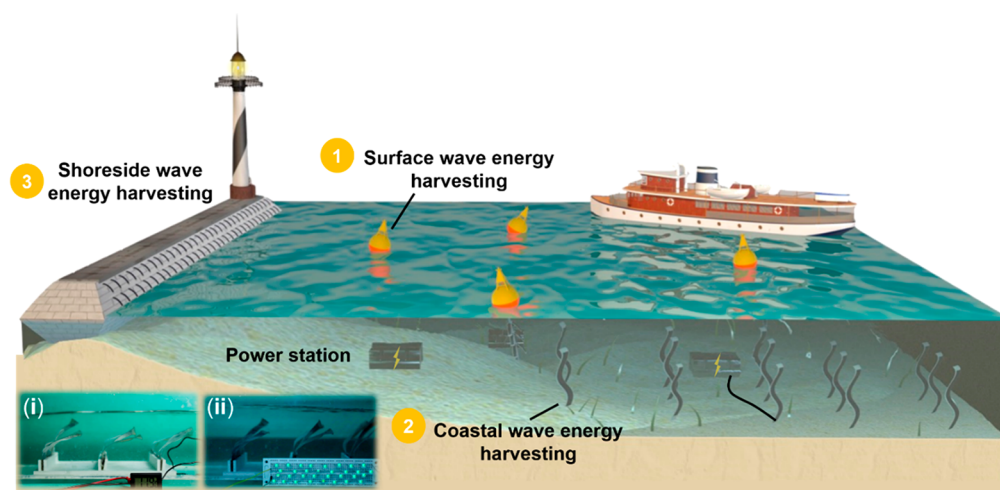


Figure 5. Illustration of various applications for S-TENG with insets of (i) the thermometer powered by nine S-TENGs and (ii) 30 LEDs powered by nine S-TENGs.

The current and the power density of the S-TENG at different load resistances are shown in Figure S6. It can be observed that, under the matched loading resistance (20 M Ω in this case), the peak output power of the S-TENG reached a maximum of 10.56 μ W. Through a series of experiments performed with different charging capacitors (Figure S7), the S-TENG yields a generally good charging capability for the capacitors. The experiments testing the output performance with different salinities are conducted as shown in Figure S8. It can be observed that the output performance is not significantly affected by the salinity. As shown in Table S3, some previous wave energy harvesting TENGs have been reviewed and summarized. The performance of the S-TENG is not inferior in low wave frequency conditions.

As underwater structures are subject to hydrostatic pressure, it is necessary to study the effect of the underwater pressure on the output performance of the S-TENG. The wave vertical displacements are typically on the order of 10 m or so.⁵⁷ Once the water depth exceeds 10 m, there are almost no waves. In the study, different mass blocks have been rigidly installed onto the S-TENG to increase its surface pressure from 10 to 100 kPa, as shown in Figure S9. Another mass block, which will be released from the same height to create the same impact on the lower mass block and the S-TENG, hangs on top of them. Basically, under higher pressure underwater, the air gap in the S-TENG becomes more and more compressed. Consequently, the output current decreases with the underwater pressure as shown in Figure 4e, which is consistent with eq 1. However, the electrical output from the S-TENG will not be eliminated as the contact and separation of the microstructures on the electrode and dielectric material continues (Figure S9). It indicates that the S-TENG can be used to harvest wave energy at different water pressure conditions.

As the electrical performance can be enhanced by connecting multiple TENGs in parallel,^{32,58,59} experimental studies (see Figure 4f) were performed to determine the distance between multiple S-TENGs. The vibration state of two S-TENGs is different when the distance between them is within a certain value. A complete process is simulated by COMSOL to illustrate the vibration difference of two S-TENGs as shown in Figure S10 and Note S1, and experiments with different distances are conducted as shown in Figure 4f. In the simulation, the fluid speed (U) is 0.5 m/s and varies

sinusoidally with time to simulate the sinusoidal wave velocity. T is the wave period, which equals 20 s. The simulation is performed with a fluid-structure interaction model. In the COMSOL simulation, the two S-TENG units are installed with distances of 60, 90, and 120 mm, respectively. As shown in Figure S10a, in the case where the distance between the two S-TENGs is 60 mm, the forward S-TENG vibrates more severely than the back S-TENG. This can be partly attributed to the attenuation to the incident wave by the forward TENG, which can be considered as an interference between the two S-TENGs. However, as the distance of two S-TENG units increases to 90 and 120 mm, the attenuation to the vibration of the back S-TENG by the forward TENG becomes less significant, as shown in Figure S10b,c. The results indicate that the distance between two S-TENGs influences the vibration of each S-TENG. Actually, the transferred charge of the S-TENG increased before the distance between the two S-TENGs reached 120 mm, as shown in Figure 4f. Therefore, the distance between the two S-TENGs has been kept above 90 mm to eliminate their interference in the subsequent experiments.

To boost the total output, a system with multiple S-TENGs integrated has been developed. It can be observed in Figure 4g that, as the number of the S-TENG units increased from 1 to 9, the output voltage of the parallel connected S-TENGs increased from 24.8 to 120.6 V at the same time the output current increased from 2.6 to 8.7 μ A as depicted in Figure 4h. The open-circuit voltage, short-circuit current, and output power were measured with different units connected in parallel. All three signals increased with increasing units, as shown in Figure 4g–i. However, this might be contradictory, as voltage should not have increased when the units are connected in parallel. This is due to the actual voltage decreasing with the increase of units. The explanation is demonstrated in Figure S11 and Note S2. This indicates that higher power could be achieved by simply integrating more units, which is also found by Zhang *et al.*²⁹ and Xu and co-workers.⁴³ The peak output power of the nine S-TENGs reached 79.023 μ W as shown in Figure 4i; the detailed information is shown in Figure S12. Some sensors involved in MIoT and their power consumption are listed in Figure S13. When a sufficient number of S-TENGs are implemented, various MIoT sensors (*e.g.*, sonic wave loggers) can be driven.

Demonstrations of the S-TENG Applications. Owing to its flexible structure, the S-TENG can be easily integrated with a variety of marine applications (Figure 5), including surface (e.g., floating buoys) and shoreside (e.g., lighthouses, coastal power stations) applications.

Buoys and floats carry a large number of sensors, which form the nerve endings in the marine internet of things. The S-TENG can be integrated with a floating buoy very easily (Figure S14). In the demonstration experiments, as the wave excited the vibration of the S-TENG, the high brightness LEDs on the floating buoy flashed continuously (see Movie S1). By integrating with similar S-TENGs, these buoy-based sensors could achieve robust (in ocean environments) and low-cost battery independence.

As the marine internet of things extends to underwater areas, power supply without a battery is even more challenging (where solar and wind energy are not available at all). Our demonstration experiments have also explored the applicability of the S-TENG in this scenario, in which S-TENGs form a coastal power station (Figure 5). In the experiments performed in a flume with a dimension of 2.0 m (length) \times 0.3 m (width) \times 0.5 m (height), a 100 μ F capacitor was charged to 3 V in 100 s by nine S-TENGs; then, a thermometer was successfully lit up (as shown in Figures 5(i) and S15 and Movie S2). This “mini” S-TENG power station was also capable of lighting up 30 LEDs (Figure 5(ii) and Movie S3), which demonstrates the S-TENG’s applicability under water.

Last but not least, the S-TENG can also be installed at the shoreside areas to power a series of coastal applications (see Figure 5). As a demonstration, 3 S-TENGs were attached to a breakwater model (see Figure S16(i)) to power a coastal lighthouse model (see Figure S16(ii) and Movie S4). The S-TENG yielded quite stable (for more than 6 h) electrical performance (Figure S17). Through these experimental demonstrations, the flexible S-TENG proves to be effective in various marine scenarios.

CONCLUSION

In this study, a flexible seaweed-like triboelectric nanogenerator has been developed and investigated in systematic wave tank experiments. Studies reveal that, depending on the geometric parameter (*i.e.*, the aspect ratio) and dynamic parameter (*i.e.*, the Strouhal number), the vibration of the S-TENG can develop into two modes. The S-TENG proves to be an effective wave energy converter when it vibrates in the first mode. When multiple S-TENGs are deployed appropriately (*i.e.*, with proper distance in between each other), the total electric output can be promoted by simply integrating more parallel connected S-TENG units. Therefore, a series of demonstration experiments were performed in a wave tank, in which multiple S-TENGs have proven to be effective in powering the LEDs and the thermometer in different marine scenarios. Considering that the majority of the MIoT sensors work with micro power, the essentially robust and cost-efficient S-TENG could become an effective approach to achieve battery independence for the MIoT.

METHODS

Manufacture of the S-TENG. The structure of the S-TENG is shown in Figure 1a(iii). The FEP and PET membranes and PTFE sealing tape had the thicknesses of 30, 20, and 30 μ m, respectively. The two flexible electrodes were composed by an ink-coated FEP and an ink-coated PET, and they were integrated with the sealing PTFE.

The conductive ink No. is CH-8(MOD2) produced by JUJO printing supplies and technology (Pinghu) Co. Ltd. The conductive ink is printed on the FEP and PET membranes by the screen-printing technology and then dried at atmospheric temperature. There is an air gap between the ink-coated PET film and the FEP membrane. A double-side adhesive sponge belt (3 mm thickness) is set at the root of the S-TENG to separate the ink-coated PET film and the FEP film as shown in Figure 1a(iii). The surface of the FEP membrane and ink-coated PET film was lightly polished with 10 000 mesh sandpaper from Kafuwel Co., Ltd.

Characterization of the Materials Used in S-TENG. The microstructure of the FEP and ink-coated PET film can be observed by a scanning electron microscope Phenom Pro as shown in Figure 2a(ii). Material surface morphologies of the conductive ink-coated PET film and FEP film are observed with the electron microscope LEXT OLS4000, which is shown in Figure S1. Figure 1b(i,ii) shows the sample, and Figure 1b(iii) shows the material surface morphology of the S-TENG, which yields an air gap between the FEP film and the ink-coated PET film.

Electrical Output Measurement. A programmable electrometer (Keithley Model 6514) was used to measure the electrical output of the S-TENG. A wave simulation system, consisting of an adjustable velocity motor (US-52) equipped with a reduction gearbox (SGU-5-K MAILI), was used to simulate the water wave motion. The demonstration experiments for the S-TENG were performed with a 2.0 m (length) \times 0.3 m (width) \times 0.5 m (height) flume. The simulated wave velocity ranged from 0.04 to 0.4 m/s.

Demonstration Experiments Done by S-TENG. In the demonstration experiments, the S-TENG was installed on a bedplate, which is shown in Figure 5(i),(ii). The wave was generated as the linear motor pushed/pulled the wave-making plate back and forth. When the S-TENG is excited by waves, the periodic electrical signals can be generated as shown in Figures 3c,d and 4.

ASSOCIATED CONTENT

Supporting Information

The Supporting Information is available free of charge at <https://pubs.acs.org/doi/10.1021/acsnano.1c05127>.

Tables S1–S3: physical properties of the materials; experimental data for bending behavior; a summary of output performance and working wave frequency of various wave energy harvesting TENGs; Figures S1–S17: material surface morphology of the ink-coated PET film and FEP film measured by a scanning electron microscope; coordinate system of the S-TENG; corresponding electric potential distributions for the S-TENG; effect of the linear motor amplitude on the transferred charge of the S-TENG; effect of the linear motor frequency on the transferred charge and output power of the S-TENG; dependence of the output current and power on the external resistance; charging rate for different capacitors of the S-TENG; output performance comparison of the S-TENG on the open-circuit voltage, short-circuit current, and transferred charge with different salinities; experimental apparatus to study the effect of the underwater pressure on the output performance of the S-TENG; velocity distribution around the two S-TENGs during a quarter of the wave period; electric-circuit model of the multiple S-TENGs; dependence of the output current and power on the external resistance of the nine S-TENG units; power consumption of the common sensors in MIoT; S-TENGs integrated with floating buoy; powering a thermometer with nine S-TENGs; powering a lighthouse model with three S-TENGs; durability test of the S-TENG; Notes S1–S2: simulation of two S-TENGs

excited by the wave; influence of the effect of multiple units on the device of output voltage (PDF)
Movie S1: S-TENG integrated with a floating buoy to power an indicating light (MP4)
Movie S2: S-TENGs to power a thermometer (MP4)
Movie S3: S-TENGs to power 30 LEDs (MP4)
Movie S4: S-TENGs installed on the breakwater to power a lighthouse (MP4)

AUTHOR INFORMATION

Corresponding Authors

Minyi Xu – Dalian Key Laboratory of Marine Micro/Nano Energy and Self-powered Systems, Marine Engineering College, Dalian Maritime University, Dalian 116026, China; orcid.org/0000-0002-3772-8340; Email: xuminyi@dlmu.edu.cn

Zhong Lin Wang – Beijing Institute of Nanoenergy and Nanosystems, Chinese Academy of Sciences, Beijing 100083, China; School of Materials Science and Engineering, Georgia Institute of Technology, Atlanta, Georgia 30332-0245, United States; orcid.org/0000-0002-5530-0380; Email: zlwang@gatech.edu

Authors

Yan Wang – Dalian Key Laboratory of Marine Micro/Nano Energy and Self-powered Systems, Marine Engineering College, Dalian Maritime University, Dalian 116026, China

Xiangyu Liu – Dalian Key Laboratory of Marine Micro/Nano Energy and Self-powered Systems, Marine Engineering College, Dalian Maritime University, Dalian 116026, China

Yawei Wang – Dalian Key Laboratory of Marine Micro/Nano Energy and Self-powered Systems, Marine Engineering College, Dalian Maritime University, Dalian 116026, China

Hao Wang – Dalian Key Laboratory of Marine Micro/Nano Energy and Self-powered Systems, Marine Engineering College, Dalian Maritime University, Dalian 116026, China

He Wang – Dalian Key Laboratory of Marine Micro/Nano Energy and Self-powered Systems, Marine Engineering College, Dalian Maritime University, Dalian 116026, China

Steven L. Zhang – School of Materials Science and Engineering, Georgia Institute of Technology, Atlanta, Georgia 30332-0245, United States; Robotic Materials Department, Max Planck Institute for Intelligent Systems, Stuttgart 70569, Germany

Tiancong Zhao – School of Marine Engineering and Technology, Sun Yat-sen University, Guangzhou, Guangdong 510275, China

Complete contact information is available at:
<https://pubs.acs.org/10.1021/acsnano.1c05127>

Author Contributions

[‡]Y.W., X.Y.L., and Y.W.W. contributed equally to this work. M.Y.X. and Z.L.W. conceived the idea and designed the experiments. Y.W., X.Y.L., Y.W.W., and He Wang fabricated the devices and performed the experiments. S.L.Z. and T.C.Z. provided suggestions for the experiments. Y.W., X.Y.L., Y.W.W., Hao Wang, M.Y.X., and Z.L.W. wrote the manuscript. All the authors discussed the results and commented on the manuscript.

Funding

The work was supported by the National Natural Science Foundation of China (Grant No. 51879022, 51979045, and

51906029), the Fundamental Research Funds for the Central Universities, China (Grant No. 3132019330), and the China Scholarship Council (CSC No. 202006570022).

Notes

The authors declare no competing financial interest.

REFERENCES

- (1) Xu, G.; Shi, Y.; Sun, X.; Shen, W. Internet of Things in Marine Environment Monitoring: A Review. *Sensors* **2019**, *19*, 1711.
- (2) Hu, C.; Pu, Y.; Yang, F.; Zhao, R.; Alrawais, A.; Xiang, T. Secure and Efficient Data Collection and Storage of IoT in Smart Ocean. *IEEE Internet Things J.* **2020**, *7*, 9980–9994.
- (3) Toma, D. M.; O'Reilly, T.; del Rio, J.; Headley, K.; Manuel, A.; Broring, A.; Edgington, D. Smart Sensors for Interoperable Smart Ocean Environment. In *OCEANS IEEE - Spain*, 2011; pp 1–4; DOI: [10.1109/Oceans-Spain.2011.6003654](https://doi.org/10.1109/Oceans-Spain.2011.6003654).
- (4) Qiu, T.; Zhao, Z.; Zhang, T.; Chen, C.; Chen, C. L. P. Underwater Internet of Things in Smart Ocean: System Architecture and Open Issues. *IEEE T. Ind. Inform.* **2020**, *16*, 4297–4307.
- (5) Howe, B. M.; Chao, Y.; Arabshahi, P.; Roy, S.; McGinnis, T.; Gray, A. A Smart Sensor Web for Ocean Observation: Fixed and Mobile Platforms, Integrated Acoustics. *Satellites and Predictive Modeling. IEEE J-STARS* **2010**, *3*, 507–521.
- (6) Thorpe, T. W. *A Brief Review of Wave Energy*; The UK Department of Trade and Industry: Oxfordshire UK, 1999; pp ETSU-R120.
- (7) Falnes, J. A Review of Wave-Energy Extraction. *Mar. Struct.* **2007**, *20*, 185–201.
- (8) Westwood, A. Ocean Power: Wave and Tidal Energy Review. *Refocus* **2004**, *5*, 50–55.
- (9) Salter, S. H. *Nature* **1974**, *249*, 720–724.
- (10) Kofoed, J. P.; Frigaard, P.; Friis-Madsen, E.; Sørensen, H. C. Prototype Testing of the Wave Energy Converter Wave Dragon. *Renewable Energy* **2006**, *31*, 181–189.
- (11) Khan, U.; Kim, S. W. Triboelectric Nanogenerators for Blue Energy Harvesting. *ACS Nano* **2016**, *10*, 6429–32.
- (12) Marsh, G. Wave and Tidal Power — An Emerging New Market for Composites. *Reinf. Plast.* **2009**, *53*, 20–24.
- (13) Wang, X.; Niu, S.; Yin, Y.; Yi, F.; You, Z.; Wang, Z. L. Triboelectric Nanogenerator Based on Fully Enclosed Rolling Spherical Structure for Harvesting Low-Frequency Water Wave Energy. *Adv. Energy Mater.* **2015**, *5*, 1501467.
- (14) Feng, L.; Liu, G.; Guo, H.; Tang, Q.; Pu, X.; Chen, J.; Wang, X.; Xi, Y.; Hu, C. Hybridized Nanogenerator Based on Honeycomb-Like Three Electrodes for Efficient Ocean Wave Energy Harvesting. *Nano Energy* **2018**, *47*, 217–223.
- (15) Zhang, S. L.; Jiang, Q.; Wu, Z.; Ding, W.; Zhang, L.; Alshareef, H. N.; Wang, Z. L. Energy Harvesting-Storage Bracelet Incorporating Electrochemical Microsupercapacitors Self-Charged from a Single Hand Gesture. *Adv. Energy Mater.* **2019**, *9*, 1900152.
- (16) Xu, M.; Wang, P.; Wang, Y.; Zhang, S. L.; Wang, A. C.; Zhang, C.; Wang, Z.; Pan, X.; Wang, Z. L. A Soft and Robust Spring Based Triboelectric Nanogenerator for Harvesting Arbitrary Directional Vibration Energy and Self-Powered Vibration Sensing. *Adv. Energy Mater.* **2018**, *8*, 1702432.
- (17) Wang, Y.; Wang, J.; Xiao, X.; Wang, S.; Phan, T. K.; Dong, J.; Mi, J.; Pan, X.; Wang, H.; Xu, M. Multi-Functional Wind Barrier Based on Triboelectric Nanogenerator for Power Generation, Self-Powered Wind Speed Sensing and Highly Efficient Windshield. *Nano Energy* **2020**, *73*, 104736.
- (18) Xu, M.; Wang, Y.; Zhang, S. L.; Ding, W.; Cheng, J.; He, X.; Zhang, P.; Wang, Z.; Pan, X.; Wang, Z. L. An Aeroelastic Flutter Based Triboelectric Nanogenerator as a Self-Powered Active Wind Speed Sensor in Harsh Environment. *Extrem. Mech. Lett.* **2017**, *15*, 122–129.
- (19) Zhao, H.; Xiao, X.; Xu, P.; Zhao, T.; Song, L.; Pan, X.; Mi, J.; Xu, M.; Wang, Z. L. Dual-Tube Helmholtz Resonator-Based

Triboelectric Nanogenerator for Highly Efficient Harvesting of Acoustic Energy. *Adv. Energy Mater.* **2019**, *9*, 1902824.

(20) Xu, M.; Wang, S.; Zhang, S. L.; Ding, W.; Kien, P. T.; Wang, C.; Li, Z.; Pan, X.; Wang, Z. L. A Highly-Sensitive Wave Sensor Based on Liquid-Solid Interfacing Triboelectric Nanogenerator for Smart Marine Equipment. *Nano Energy* **2019**, *57*, 574–580.

(21) Jeon, S. B.; Kim, S.; Park, S. J.; Seol, M. L.; Kim, D.; Yong, K. C.; Choi, Y. K. Self-Powered Electro-Coagulation System Driven by a Wind Energy Harvesting Triboelectric Nanogenerator for Decentralized Water Treatment. *Nano Energy* **2016**, *28*, 288–295.

(22) Lu, C.; Chen, J.; Jiang, T.; Gu, G.; Tang, W. A Stretchable, Flexible Triboelectric Nanogenerator for Self-Powered Real-Time Motion Monitoring. *Adv. Mater. Technol.* **2018**, *3*, 1800021.

(23) Bian, Y.; Jiang, T.; Xiao, T.; Gong, W.; Cao, X.; Wang, Z.; Wang, Z. L. Triboelectric Nanogenerator Tree for Harvesting Wind Energy and Illuminating in Subway Tunnel. *Adv. Mater. Technol.* **2018**, *3*, 1700317.

(24) Jie, Y.; Jia, X.; Zou, J.; Chen, Y.; Wang, N.; Wang, Z. L.; Cao, X. Natural Leaf Made Triboelectric Nanogenerator for Harvesting Environmental Mechanical Energy. *Adv. Energy Mater.* **2018**, *8*, 1703133.

(25) Zou, J.; Zhang, M.; Huang, J.; Bian, J.; Jie, Y.; Willander, M.; Cao, X.; Wang, N.; Wang, Z. L. Coupled Supercapacitor and Triboelectric Nanogenerator Boost Biomimetic Pressure Sensor. *Adv. Energy Mater.* **2018**, *8*, 1702671.

(26) Xi, Y.; Guo, H.; Zi, Y.; Li, X.; Wang, J.; Deng, J.; Li, S.; Hu, C.; Cao, X.; Wang, Z. L. Multifunctional TENG for Blue Energy Scavenging and Self-Powered Wind-Speed Sensor. *Adv. Energy Mater.* **2017**, *7*, 1602397.

(27) Wang, Y.; Yang, E.; Chen, T.; Wang, J.; Hu, Z.; Mi, J.; Pan, X.; Xu, M. A Novel Humidity Resisting and Wind Direction Adapting Flag-Type Triboelectric Nanogenerator for Wind Energy Harvesting and Speed Sensing. *Nano Energy* **2020**, *78*, 105279.

(28) Zhang, S. L.; Roach, D. J.; Xu, S.; Wang, P.; Zhang, W.; Qi, H. J.; Wang, Z. L. Electromagnetic Pulse Powered by a Triboelectric Nanogenerator with Applications in Accurate Self-Powered Sensing and Security. *Adv. Mater. Technol.* **2020**, *5*, 2000368.

(29) Zhang, Y.; Zeng, Q.; Wu, Y.; Wu, J.; Yuan, S.; Tan, D.; Hu, C.; Wang, X. An Ultra-Durable Windmill-Like Hybrid Nanogenerator for Steady and Efficient Harvesting of Low-Speed Wind Energy. *Nano-Micro Lett.* **2020**, *12*, 175.

(30) Xiao, T.; Liang, X.; Jiang, T.; Xu, L.; Shao, J.; Nie, J.; Bai, Y.; Zhong, W.; Wang, Z. L. Spherical Triboelectric Nanogenerators Based on Spring-Assisted Multilayered Structure for Efficient Water Wave Energy Harvesting. *Adv. Funct. Mater.* **2018**, *28*, 1802634.

(31) Kim, D. Y.; Kim, H. S.; Kong, D. S.; Choi, M.; Kim, H. B.; Lee, J.-H.; Murillo, G.; Lee, M.; Kim, S. S.; Jung, J. H. Floating Buoy-Based Triboelectric Nanogenerator for an Effective Vibrational Energy Harvesting from Irregular and Random Water Waves in Wild Sea. *Nano Energy* **2018**, *45*, 247–254.

(32) Liang, X.; Jiang, T.; Feng, Y.; Lu, P.; An, J.; Wang, Z. L. Triboelectric Nanogenerator Network Integrated with Charge Excitation Circuit for Effective Water Wave Energy Harvesting. *Adv. Energy Mater.* **2020**, *10*, 2002123.

(33) Guo, H.; Leng, Q.; He, X.; Wang, M.; Chen, J.; Hu, C.; Xi, Y. A Triboelectric Generator Based on Checker-Like Interdigital Electrodes with a Sandwiched PET Thin Film for Harvesting Sliding Energy in All Directions. *Adv. Energy Mater.* **2015**, *5*, 1400790.

(34) Yang, X.; Chan, S.; Wang, L.; Daoud, W. A. Water Tank Triboelectric Nanogenerator for Efficient Harvesting of Water Wave Energy over a Broad Frequency Range. *Nano Energy* **2018**, *44*, 388–398.

(35) Wang, Z. L. Catch Wave Power in Floating Nets. *Nature* **2017**, *542*, 159–160.

(36) Wang, X.; Wen, Z.; Guo, H.; Wu, C.; He, X.; Lin, L.; Cao, X.; Wang, Z. L. Fully Packaged Blue Energy Harvester by Hybridizing a Rolling Triboelectric Nanogenerator and an Electromagnetic Generator. *ACS Nano* **2016**, *10*, 11369–11376.

(37) Zhang, S. L.; Xu, M.; Zhang, C.; Wang, Y.; Zou, H.; He, X.; Wang, Z.; Wang, Z. L. Rationally Designed Sea Snake Structure Based Triboelectric Nanogenerators for Effectively and Efficiently Harvesting Ocean Wave Energy with Minimized Water Screening Effect. *Nano Energy* **2018**, *48*, 421–429.

(38) Chen, B. D.; Tang, W.; He, C.; Deng, C. R.; Yang, L. J.; Zhu, L. P.; Chen, J.; Shao, J. J.; Liu, L.; Wang, Z. L. Water Wave Energy Harvesting and Self-Powered Liquid-Surface Fluctuation Sensing Based on Bionic-Jellyfish Triboelectric Nanogenerator. *Mater. Today* **2018**, *21*, 88–97.

(39) Cheng, P.; Guo, H.; Wen, Z.; Zhang, C.; Yin, X.; Li, X.; Liu, D.; Song, W.; Sun, X.; Wang, J.; Wang, Z. L. Largely Enhanced Triboelectric Nanogenerator for Efficient Harvesting of Water Wave Energy by Soft Contacted Structure. *Nano Energy* **2019**, *57*, 432–439.

(40) Lei, R.; Zhai, H.; Nie, J.; Zhong, W.; Bai, Y.; Liang, X.; Xu, L.; Jiang, T.; Chen, X.; Wang, Z. L. Butterfly-Inspired Triboelectric Nanogenerators with Spring-Assisted Linkage Structure for Water Wave Energy Harvesting. *Adv. Mater. Technol.* **2019**, *4*, 1800514.

(41) Pan, L.; Wang, J.; Wang, P.; Gao, R.; Wang, Y.-C.; Zhang, X.; Zou, J.-J.; Wang, Z. L. Liquid-FEP-Based U-Tube Triboelectric Nanogenerator for Harvesting Water-Wave Energy. *Nano Res.* **2018**, *11*, 4062–4073.

(42) Xi, Y.; Wang, J.; Zi, Y.; Li, X.; Han, C.; Cao, X.; Hu, C.; Wang, Z. High Efficient Harvesting of Underwater Ultrasonic Wave Energy by Triboelectric Nanogenerator. *Nano Energy* **2017**, *38*, 101–108.

(43) Zhong, W.; Xu, L.; Wang, H.; Li, D.; Wang, Z. L. Stacked Pendulum-Structured Triboelectric Nanogenerators for Effectively Harvesting Low-Frequency Water Wave Energy. *Nano Energy* **2019**, *66*, 104108.

(44) Xu, L.; Jiang, T.; Lin, P.; Shao, J.; He, C.; Zhong, W.; Chen, X.; Wang, Z. L. Coupled Triboelectric Nanogenerator Networks for Efficient Water Wave Energy Harvesting. *ACS Nano* **2018**, *12*, 1849–1858.

(45) Xia, K.; Fu, J.; Xu, Z. Multiple-Frequency High-Output Triboelectric Nanogenerator Based on a Water Balloon for All-Weather Water Wave Energy Harvesting. *Adv. Energy Mater.* **2020**, *10*, 2000426.

(46) Xu, M.; Zhao, T.; Wang, C.; Zhang, S. L.; Li, Z.; Pan, X.; Wang, Z. L. High Power Density Tower-Like Triboelectric Nanogenerator for Harvesting Arbitrary Directional Water Wave Energy. *ACS Nano* **2019**, *13*, 1932–1939.

(47) An, J.; Wang, Z.; Jiang, T.; Liang, X.; Wang, Z. L. Whirling-Folded Triboelectric Nanogenerator with High Average Power for Water Wave Energy Harvesting. *Adv. Funct. Mater.* **2019**, *29*, 1904867.

(48) Ouyang, H.; Tian, J.; Sun, G.; Zou, Y.; Liu, Z.; Li, H.; Zhao, L.; Shi, B.; Fan, Y.; Fan, Y.; Wang, Z. L.; Li, Z. Self-Powered Pulse Sensor for Antidiastole of Cardiovascular Disease. *Adv. Mater.* **2017**, *29*, 1703456.

(49) Niu, S.; Wang, S.; Lin, L.; Liu, Y.; Zhou, Y. S.; Hu, Y.; Wang, Z. L. Theoretical Study of Contact-Mode Triboelectric Nanogenerators as an Effective Power Source. *Energy Environ. Sci.* **2013**, *6*, 3576.

(50) Xu, M.; Wu, M.; Mi, J. A New Type of Self-Excited Flapping Jets Due to a Flexible Film At the Nozzle Exit. *Exp. Therm. Fluid Sci.* **2019**, *106*, 226–233.

(51) Eloy, C.; Lagrange, R.; Souilliez, C.; Schouveiler, L. Aeroelastic Instability of Cantilevered Flexible Plates in Uniform Flow. *J. Fluid Mech.* **2008**, *611*, 97–106.

(52) Connell, B. S. H.; Yue, D. K. P. Flapping Dynamics of A Flag in a Uniform Stream. *J. Fluid Mech.* **2007**, *581*, 33–67.

(53) Orrego, S.; Shoele, K.; Ruas, A.; Doran, K.; Caggiano, B.; Mittal, R.; Kang, S. H. Harvesting Ambient Wind Energy with an Inverted Piezoelectric Flag. *Appl. Energy* **2017**, *194*, 212–222.

(54) Wang, Z. L. Triboelectric Nanogenerators as New Energy Technology for Self-Powered Systems and as Active Mechanical and Chemical Sensors. *ACS Nano* **2013**, *7*, 9533–9557.

(55) Wang, Z. L.; Wang, A. C. On the Origin of Contact-Electrification. *Mater. Today* **2019**, *30*, 34–51.

(56) Li, H.; Ekici, K. Aeroelastic Modeling of a Three-Dimensional Wing Using the Harmonic-Balance-Based One-Shot Method. In *AIAA Scitech Forum*, San Diego, CA, January 7–11, 2019; DOI: [10.2514/6.2019-0607](https://doi.org/10.2514/6.2019-0607).

(57) Garrett, C. Internal Waves. In *Encyclopedia of Ocean Sciences*, Second ed.; Steele, J. H., Ed. Academic Press: Oxford, 2001; pp 266–273.

(58) Li, X.; Tao, J.; Wang, X.; Zhu, J.; Pan, C.; Wang, Z. L. Networks of High Performance Triboelectric Nanogenerators Based on Liquid-Solid Interface Contact Electrification for Harvesting Low-Frequency Blue Energy. *Adv. Energy Mater.* **2018**, *8*, 1800705.

(59) Wang, H.; Xu, L.; Bai, Y.; Wang, Z. L. Pumping Up the Charge Density of a Triboelectric Nanogenerator by Charge-Shuttling. *Nat. Commun.* **2020**, *11*, 4203.